Supplementary material associated with the article "Quantifying resolution limiting factors in subtomogram averaged cryo-electron tomography using simulations"

Lenard M. Voortman[a], Miloš Vulović[a,b], Massimiliano Maletta[c], Andreas Voigt[d], Erik M. Franken[d], Angelita Simonetti[e], Peter J. Peters[c], Lucas J. van Vliet[a], Bernd Rieger[a]

[a] *Quantitative Imaging Group, Department of Imaging Physics, Delft University of Technology, Lorentzweg 1, 2628 CJ Delft, The Netherlands*
[b] *Electron Microscopy Section, Molecular Cell Biology, Leiden University Medical Center, P.O.Box 9600, 2300 RC Leiden, The Netherlands*
[c] *NKI Netherlands Cancer Institute - Antoni van Leeuwenhoek Hospital, Plesmanlaan 121 B6, 1066 CX Amsterdam, The Netherlands*
[d] *FEI Company, Achtseweg Noord 5, 5651 GG Eindhoven, The Netherlands*
[e] *Architecture et Réactivité de l'ARN, Université de Strasbourg, CNRS, IBMC, 67084 Strasbourg Cedex, France*

1. Predicting the influence of CTF correction and defocus estimation

1.1. CTF correction

The CTF inherently depends on the amount defocus, and the defocus varies over the specimen along the optical axis. Owing to the specific geometry associated with cryo-electron tomography (CET), special CTF correction methods have been developed. The tilting of a (thin) specimen results in a defocus gradient across the image, perpendicular to the tilt-axis. Furthermore, depending on the thickness, the image contributions from the top and bottom of the specimen can exhibit a significant difference in defocus.

CTF correction methods for tomography can be categorized into three groups.

First, the most basic form ignores the defocus gradient. We will refer to this method as regular CTF model (CTF0):

$$\hat{I}_{\mathrm{CTF0}}(\mathbf{q}) = ie^{-i\chi(q)}\hat{V}_\alpha(\mathbf{q},0) - ie^{i\chi(q)}\hat{V}_\alpha(\mathbf{q},0), \quad (1)$$

where $\mathbf{q}=(q_x,q_y)$, $\hat{I}(\mathbf{q})$ is the Fourier transform of the image intensity $I(\mathbf{x})$ and $\hat{V}_\alpha(\mathbf{q},q_z)$ is the Fourier transform of the 3D scattering potential V in a rotated coordinate system, i.e. $\hat{V}_\alpha(\mathbf{q},0)$ is a projection slice of $\hat{V}$ at tilt angle α. Furthermore, $\chi(q)=\frac{2\pi}{\lambda}\left(\frac{1}{4}C_s\lambda^4q^4+\frac{1}{2}\Delta f\lambda^2q^2\right)$ is the aberration function, C_s the spherical aberration, Δf the defocus at the center of the specimen, λ the electron wavelength and $q=\|\mathbf{q}\|$ the magnitude of the spatial frequency $\mathbf{q}$.

Second, CTF correction for tilted geometries has been studied in Philippsen et al. (2007); Voortman et al. (2011, 2012); Winkler and Taylor (2003); Fernández et al. (2006); Xiong et al. (2009); Zanetti et al. (2009). The analytical form of the tilted CTF (TCTF) is

$$\hat{I}_{\mathrm{TCTF}}(\mathbf{q}) = ie^{-i\chi(q)}\hat{V}_\alpha\left(\mathbf{q}-\frac{1}{2}\lambda q^2\boldsymbol{\beta}\tan\alpha,0\right) - ie^{i\chi(q)}\hat{V}_\alpha\left(\mathbf{q}+\frac{1}{2}\lambda q^2\boldsymbol{\beta}\tan\alpha,0\right), \quad (2)$$

where $\boldsymbol{\beta}$ is a unit-vector perpendicular to the tilt-axis $\boldsymbol{\beta}=(\cos\beta,\sin\beta)$ and β denotes the orientation of the tilt-axis (azimuth).

Third, the influence of the defocus gradient within the specimen (along the optical axis) has been studied by Kazantsev et al. (2010); Voortman et al. (2011, 2012); Jensen and Kornberg (2000). We will refer to this method as 3D CTF model (3DCTF):

$$\hat{I}_{\mathrm{3DCTF}}(\mathbf{q}) = ie^{-i\chi(q)}\hat{V}_\alpha\left(\mathbf{q},-\frac{1}{2}\lambda q^2\right) - ie^{i\chi(q)}\hat{V}_\alpha\left(\mathbf{q},\frac{1}{2}\lambda q^2\right). \quad (3)$$

From Eqs. (1), (2) and (3) it is clear that the difference between these CTF models can be fully characterized by shifts in the Fourier representation of the potential. The

difference between Eqs. (1) and (2) is a shift of $\pm\frac{1}{2}\lambda q^2 \tan\alpha$ along $\boldsymbol{\beta}$ in the Fourier domain. Similarly, the difference between Eqs. (2) and (3) is a shift of $\pm\frac{1}{2}\lambda q^2 \frac{1}{\cos\alpha}$ along q_z (Voortman et al., 2011).

Eq. (3) is the most accurate CTF model since it accounts for all defocus gradients. Eq. (1) is the least accurate but also the fastest to compute (Voortman et al., 2011). Therefore, we want to estimate the error that is introduced by approximating the 3DCTF. This error is closely related to the damping envelope we derived previously that estimates the loss of useful contrast when a specimen with finite thickness is approximated by an infinitely thin specimen (Voortman et al., 2011). This damping envelope is the result of a specific shift of sampling points in the Fourier domain.

In general, shifting in the Fourier domain results in a loss of correlation between the 'unshifted' and 'shifted' version. Similar to our previous work (Voortman et al., 2011), we approximate this correlation loss as

$$E(\boldsymbol{\Delta q}) = \mathrm{sinc}\left(d|\boldsymbol{\Delta q}|\right), \tag{4}$$

where d is the spatial extent or field-of-view and sinc is the normalized sinc function. Eq. (4) can be used to quantify the difference between CTF0, TCTF and 3DCTF correction of a projection at a specific tilt-angle, field-of-view and thickness.

For tomography, however, different projections are combined to form a 3D volume. Therefore, the differences in the reconstructed volume are an average of the differences between the projections in the tilt-series. When the specimen is tilted, the part of the field-of-view which can be used effectively for the 3D reconstruction is reduced by $1/\cos\alpha$. Then the expected correlation between a reconstruction with CTF0 and TCTF correction is given by the average

$$E_{\mathrm{CTF0}}(q) = \frac{1}{N}\sum_{n=1}^{N} \mathrm{sinc}\left(\frac{1}{2}\lambda q^2 d \sin\alpha_n\right), \tag{5}$$

where the summation is over all α_n in a tilt-series with a total of N projections.

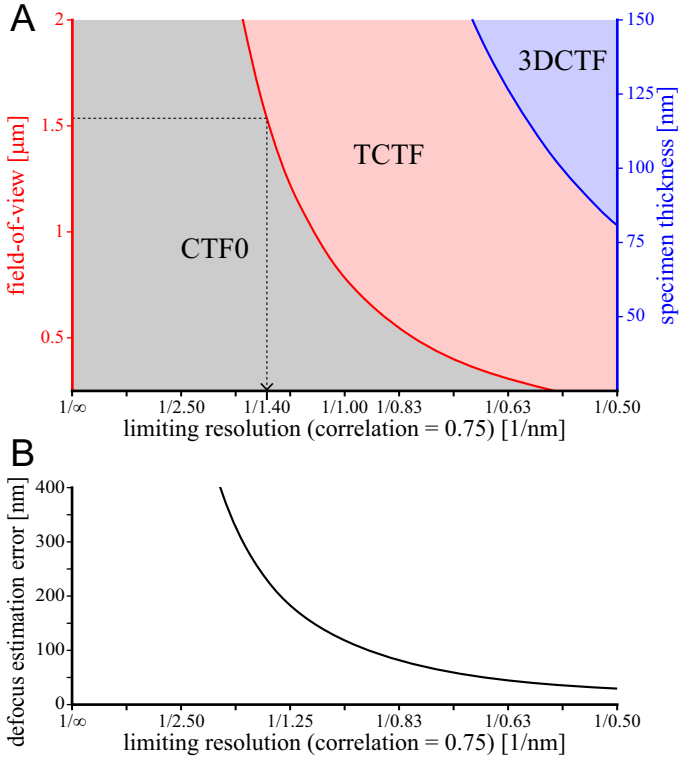

Fig. 1. (A) Regions of applicability for the different CTF correction methods. The limiting resolution was determined by thresholding the correlation functions Eqs. (5) and (6) at 0.75. From this resolution onwards the Fourier shell correlation is expected to be damped by more than 25%. Limits are presented for CTF0 correction as a function of FOV and for TCTF correction as a function of the specimen thickness, for a tilt-series of $\pm 60°$. (B) Maximum allowable defocus estimation error as a function of resolution, determined by thresholding the correlation function Eq. (7) at 0.75.

The difference between 3DCTF correction and TCTF correction depends on the thickness of the specimen. The shift of magnitude $\frac{1}{2}\lambda q^2 \frac{1}{\cos\alpha}$ is in the axial direction of the specimen's Fourier transform. Therefore the effective d is the thickness t of the specimen and the expected correlation is given by

$$E_{\mathrm{TCTF}}(q) = \frac{1}{N}\sum_{n=1}^{N} \mathrm{sinc}\left(\frac{1}{2}\lambda q^2 \frac{t}{\cos\alpha_n}\right). \tag{6}$$

We consider two CTF correction methods similar (no significant difference) when their correlation is larger than

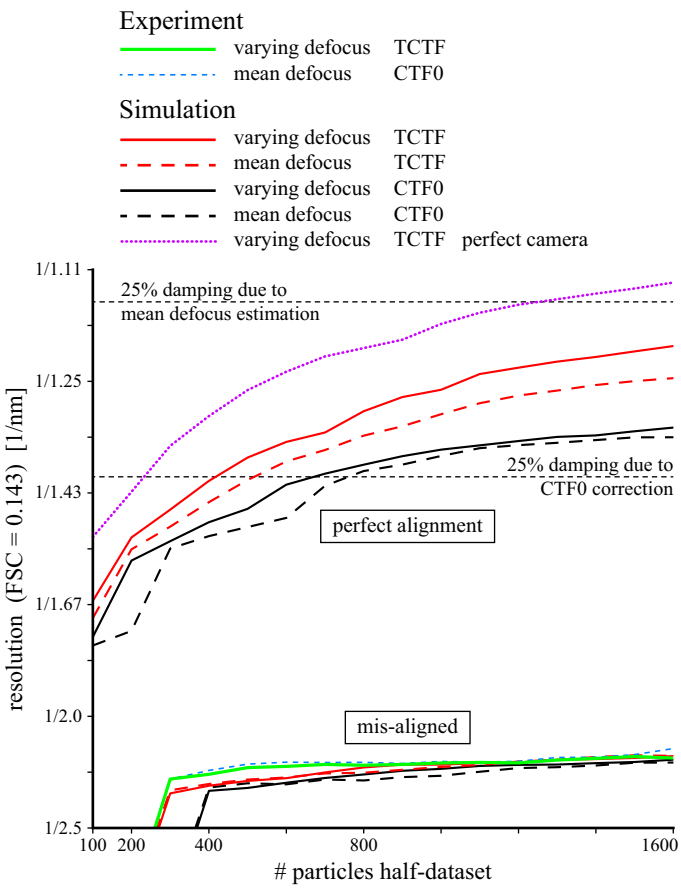

Fig. 2. A figure similar to Fig. 4. in the main text with included criteria from Fig. 1 (horizontal lines)

0.75. Thresholding the expected correlation at 0.75 we find the maximum resolution up to which we considered CTF models to be similar. Fig. 1A shows this limiting resolution for a range of field-of-views and specimen thicknesses given a tilt-series of ±60°. The choice for 0.75 as a threshold is somewhat arbitrary. However, from Fig. 2 we conclude that the choice for 0.75 does provide a good indication of the resolution at which the influence of CTF correction or defocus estimation becomes relevant. Furthermore, the relative importance of defocus estimation and CTF correction was predicted correctly using Eqs. (5), (6) and (7).

1.2. Defocus estimation

Similar to the influence of CTF correction, we predict how the accuracy of defocus estimation influences the resolution. Whereas the difference between CTF correction methods can be characterized by shifts in the Fourier domain, a difference in defocus estimation results in an extra random phase contribution to the Fourier transform of the potential. This phase translates to a correlation function

$$E_{\sigma_{\Delta f}}(q) = \cos\left(\pi\lambda q^2 \sigma_{\Delta f}\right), \qquad (7)$$

where $\sigma_{\Delta f}$ is the estimation error of the defocus Δf.

Fig. 1B shows the limiting resolution for a range of defocus estimation errors. Similar to Fig. 1A, a threshold of 0.75 was applied to Eq. (7) to find the limiting resolution.

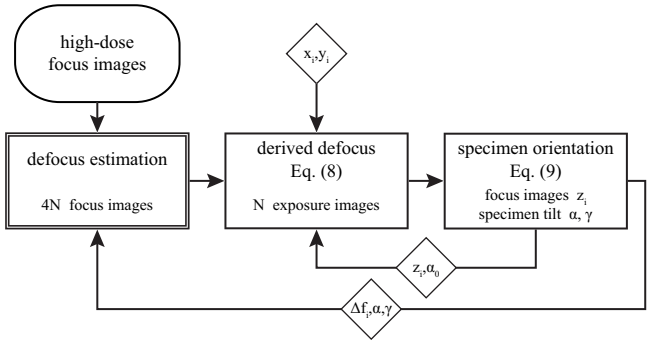

Fig. 3. Flow-diagram for theestimation of the defocus on the *exposure images* from the high-dose *focus images*. The lateral location of the focus images is given by (x_i, y_i). The axial location z_i (w.r.t. unrotated coordinate system $\alpha = 0$) is estimated from the estimated defocus and subsequently used to improve the defocus estimate.

2. Defocus estimation using extended acquisition scheme

After acquiring tilt-series using the extended acquisition scheme, the defocus at the *exposure images* can be estimated. The flow-diagram is presented in Fig. 3.

First, the defocus of the high-dose *focus images* is estimated using the methods described in Vulović et al. (2012).

Next, the defocus at the location of the *exposure images* ($\Delta f(\alpha)$) is estimated from the defocus of each *focus image* ($\Delta f_i(\alpha)$) using

$$\Delta f(\alpha) \approx \Delta f_i(\alpha) - \sin(\alpha)\, x_i - \frac{\cos(\alpha_0)}{\cos(\alpha + \alpha_0)} z_i, \qquad (8)$$

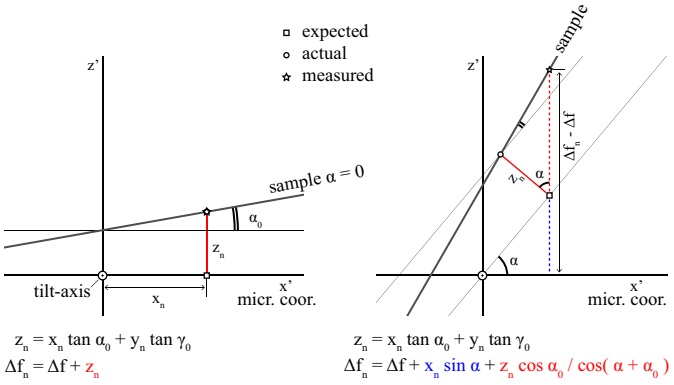

Fig. 4. Graphical representation of Eq. (8). The acquisition software accounts for the movement of the focus area (*expected*). However, due to the specimen orientation α_0, γ_0 when $\alpha = 0$, the focus area has a different location (*actual*). As a result, the *measured* defocus depends on the axial location z_i of the focus area.

where α is the tilt-angle and α_0 the specimen orientation at $\alpha = 0$. Furthermore, (x_i, y_i, z_i) is the location of the *focus image* with respect to the *exposure image* in specimen coordinates where y is aligned with the tilt-axis. For a graphical representation see Fig. 4.

However, initially Eq. (8) contains two unknowns: α_0 and z_i. Therefore, we use an iterative procedure described in Fig. 3. Using a rough estimate of $\Delta f\,(\alpha)$ we estimate z_i with

$$z_i = \text{median}_\alpha \left[\left(\Delta f_i\,(\alpha) - \Delta f\,(\alpha) - \sin(\alpha)\, x_i \right) \frac{\cos(\alpha_0 + \alpha)}{\cos(\alpha_0)} \right]. \tag{9}$$

We then refine the estimate of z_i by assuming that the specimen is (locally) a perfect plane. Using linear regression, we estimate the specimen orientation α_0, γ_0 assuming

$$z_i = \tan(\alpha_0) x_i + \tan(\gamma_0) y_i + \epsilon \quad \text{for } i = \{1, 2, 3, 4\}. \tag{10}$$

Setting $z_i = \tan(\alpha_0) x_i + \tan(\gamma_0) y_i$ refines the estimate of z_i. This regression analysis also allows us to check whether the specimen is locally flat. The inner-loop in Fig. 3 is iterated until the specimen orientation α_0, γ_0 has converged, or for a maximum of 10 iterations.

Using the defocus $\Delta f_i\,(\alpha)$ and defocus gradient estimates, we can refine the defocus estimation on the focus images (outer loop in Fig. 3). Xiong et al. (2009) introduced a method for shifting and averaging power spectra. This method is especially beneficial for high tilt-angles in the tilt-series. At these high tilt-angles the strong defocus gradient blurs the Thon rings of the power spectrum. We implemented a periodogram averaging technique which aligns the zero-crossings, given an estimate of the defocus and defocus gradient. The defocus gradient is derived from the estimated specimen orientation, taking into account the tilt-axis orientation in the images. We noticed that, for the used experimental parameters, this extra iteration was essential. The outer loop is iterated only once.

3. The influence of number of frequency shells on the reported resolution

In Fig. 3. of the main text we observe oscillations in the FSC due to the zero-crossings of the CTF. Here we demonstrate that the visibility of these dips depends on the width of the frequency shells used for calculating the FSC. Consequently, this influences the found resolution by thresholding the FSC curve.

Dips in the FSC in subtomogram averaging occur if the particles are recorded with a similar defocus. Even though each tilt-series exhibits a certain variation in defocus and each tilted projection contains macromolecules imaged with a different defocus, this defocus spread does not guarantee that the SNR around the zero-crossings is similar to all other spatial frequencies. Only when a large number of particles is averaged or when tomograms are intentionally acquired using different defoci, can these dips be avoided.

Nevertheless, Fig. 5 shows that when the number of frequency shells used to calculate the FSC is too low, it is impossible to judge whether these dips disappeared due to undersampling of the FSC or that the SNR was indeed high enough. Furthermore, choosing too few frequency shells can lead to an erroneous increase in the reported resolution.

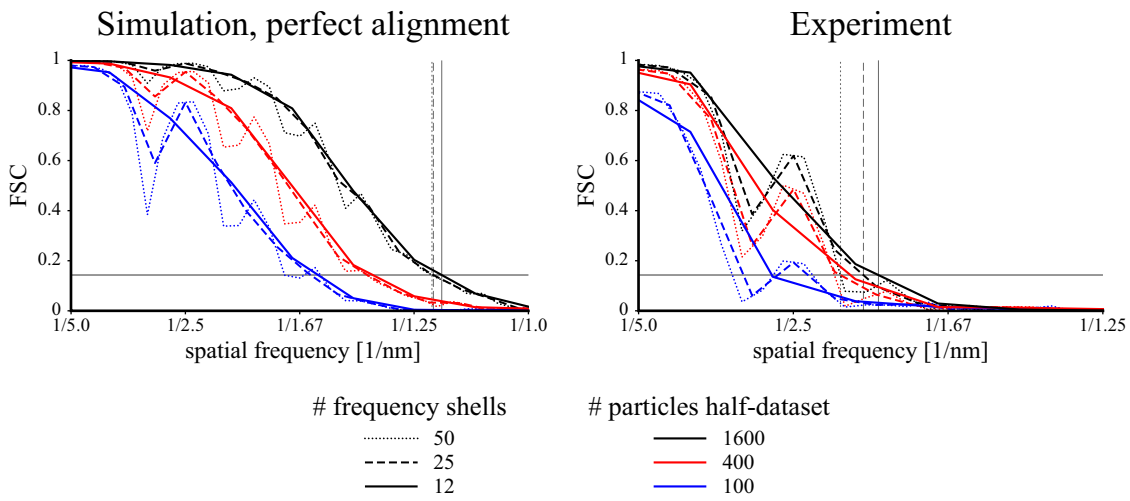

Fig. 5. Fourier Shell Correlation (FSC) for different numbers of frequency shells and numbers of particles for one simulated dataset and one experimental dataset. Both datasets are processed using TCTF correction using a varying defocus estimate. The simulated data has a perfect tilt-series alignment whereas the experimental data has a non-perfect alignment.

For the aforementioned reasons we calculate the FSC using 50 frequency shells, making the oscillations in the FSC more apparent. This number of frequency shells results in a frequency shell width that is close to the voxel size of the Fourier transformed subtomograms in this study. (size of the subtomograms was 128^3 voxels). Fig. 5 shows that due to these oscillations it is possible that the FSC crosses the threshold multiple times. We use the spatial frequency where the FSC crosses the threshold for the first time to determine the resolution.

Different choices in terms of the number of frequency shells, type of threshold and whether to use the first or last crossing of the threshold lead to different reported resolutions. The focus of this study is to quantify the influence of the different processing steps that lead to a reconstruction. Therefore, we primarily use FSC and the derived resolution to make a relative comparison between experiments and different simulations. In that sense, the choice of resolution criteria and the exact computation of the FSC does not influence our findings.

4. Experimental and simulated projections and tomogram slices

In Fig. 6 we present experimental and simulated zero-tilt projections as well as the central z-slice from the corresponding tomograms. Parameters from acquisition, processing and simulations are shown in Table 1.

References

Fernández, J.J., Li, S., Crowther, R.A., 2006. CTF determination and correction in electron cryotomography. Ultramicroscopy 106, 587–596.

Jensen, G.J., Kornberg, R.D., 2000. Defocus-gradient corrected back-projection. Ultramicroscopy 84, 57–64.

Kazantsev, I.G., Klukowska, J., Herman, G.T., Cernetic, L., 2010. Fully three-dimensional defocus-gradient corrected backprojection in cryoelectron microscopy. Ultramicroscopy 110, 1128–1142.

Philippsen, A., Engel, H.A., Engel, A., 2007. The contrast-imaging function for tilted specimens. Ultramicroscopy 107, 202–212. doi:10.1016/j.ultramic.2006.07.010.

Voortman, L.M., Franken, E.M., van Vliet, L.J., Rieger, B., 2012. Fast, spatially varying CTF correction in TEM. Ultramicroscopy 118, 26–34.

Voortman, L.M., Stallinga, S., Schoenmakers, R.H.M., van Vliet, L.J., Rieger, B., 2011. A fast algorithm for computing and correcting the CTF for tilted, thick specimens in TEM. Ultramicroscopy 111, 1029–1036.

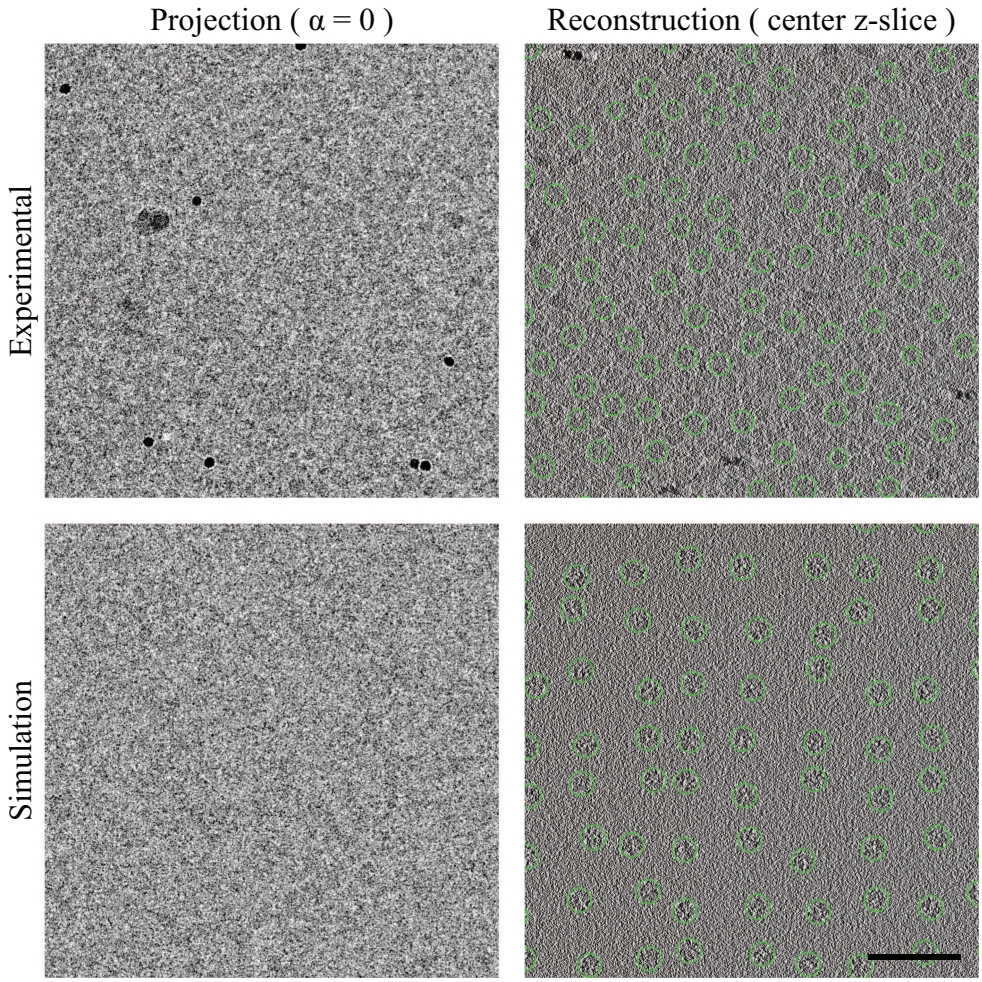

Fig. 6. An example of experimental and simulated projections, as well as slices from a tomogram. The scale bar corresponds to 100 nm (cropped image).

Vulović, M., Franken, E., Ravelli, R.B.G., van Vliet, L.J., Rieger, B., 2012. Precise and unbiased estimation of astigmatism and defocus in transmission electron microscopy. Ultramicroscopy 116, 115–134. doi:10.1016/j.ultramic.2012.03.004.

Winkler, H., Taylor, K.A., 2003. Focus gradient correction applied to tilt series image data used in electron tomography. Journal of Structural Biology 143, 24–32.

Xiong, Q., Morphew, M.K., Schwartz, C.L., Hoenger, A.H., Mastronarde, D.N., 2009. CTF determination and correction for low dose tomographic tilt series. Journal of Structural Biology 168, 378–387.

Zanetti, G., Riches, J.D., Fuller, S.D., Briggs, J.A.G., 2009. Contrast transfer function correction applied to cryo-electron tomography and sub-tomogram averaging. Journal of Structural Biology 168, 305–312.

Table 1. Acquisition, processing and simulation parameters

Parameter/type	Value
Microscope	Krios (FEI Company)
Voltage	300 kV
Spherical aberration	2.7 mm
Chromatic aberration	2.7 mm
Objective aperture	100 μm
Energy spread	0.7 eV
Illumination aperture	0.03 mrad
Requested underdefocus	0.7 eV
Detector	Falcon I (4k x 4k)
Pixel size	3.748 Å
Field-of-view	1.54 μm
Total dose	78 $e^-/Å^2$
Tilt range	$[-60°\ \ 60°]$
Angular increment	2°
PDBid (sim)	2WRI+2WRJ (70S Ribo)
Electron-specimen interaction (sim)	Thick phase grating approximation
Number of particles	3198